PHYSICAL REVIEW LETTERS **136,** 188201 (2026)

Size-Specific Transport of Colloidal Particles Using Magnetic Fields

Sebastian Wohlrab,[1] Lara Schelter,[1] Aneena Rinu Perayil,[1] Piotr Kuświk,[2] Maciej Urbaniak,[2] Feliks Stobiecki,[2]
Arne J. Vereijken,[3] Arno Ehresmann,[3] Thomas M. Fischer,[1] and Daniel de las Heras[4,1,*]
[1]*Physikalisches Institut, Universität Bayreuth, D-95440 Bayreuth, Germany*
[2]*Institute of Molecular Physics, Polish Academy of Sciences, 60-179 Poznań, Poland*
[3]*Institute of Physics and Center for Interdisciplinary Nanostructure Science and Technology (CINSaT), Universität Kassel, D-34132 Kassel, Germany*
[4]*Institute for Theoretical Physics, University of Tübingen, D-72076 Tübingen, Germany*

(Received 9 December 2025; revised 9 March 2026; accepted 10 April 2026; published 6 May 2026)

Using computer simulations and experiments, we demonstrate a mechanism for simultaneous size-specific control over the trajectories of isotropic colloidal particles. Magnetic microparticles of different diameters suspended above a periodic magnetic film are driven by loops traced by the orientation of a uniform external magnetic field. The uniform time-dependent magnetic field couples to the inhomogeneous static magnetic field of the pattern, generating a complex energy landscape for the microparticles. The energy landscape varies with height above the pattern, acting on particles of different sizes in distinct ways, as their centers are located at different elevations. At a specific elevation, distinct modulation loops exist that transport the particles to a neighboring unit cell of the pattern. The transport is topologically protected because it is determined only by a set of winding numbers of the modulation loop, which act as topological invariants. The set of winding numbers depends on the elevation, and hence, on the particle size, allowing simultaneous and independent driving of different-sized particles along arbitrarily complex and distinct trajectories.

DOI: 10.1103/nvxs-n1ml

Precise manipulation of microparticles is crucial in numerous applications, including drug delivery, cell sorting, biotesting, microassembly, and advanced material synthesis. Traditional techniques, such as optical tweezers, acoustic fields, and dielectrophoresis, provide some degree of control, but often lack the necessary selectivity and flexibility. Recent works have shown that coupling a time-dependent uniform magnetic field with a static, spatially inhomogeneous magnetic field enables highly precise control of individual magnetic microparticles suspended above periodic magnetic patterns [1–3]. The motion depends on a set of winding numbers of the modulation loop, and it is, therefore, topologically protected, making it robust against external perturbations. Beyond single particle control, simultaneous multiparticle control is possible based on (i) differences in magnetic susceptibility distinguishing paramagnetic and diamagnetic particles [1], (ii) the number of particles within a chain [4], and (iii) the particle positions above nonperiodic patterns [5]. In all these cases, transport was restricted to a plane sufficiently far above the pattern. This high-elevation limit simplifies the already complex time- and space-dependent energy landscape that drives the dynamics, facilitating a simplified theoretical modeling. However, limiting the transport to high elevations results in particle dynamics that are independent of the elevation and, therefore, of particle size. This limitation precludes applications like size-dependent sorting, which could be valuable for controlling particle dispersity, a critical parameter in cell separation [6], targeted drug delivery [7,8], and the fabrication of photonic crystals [9] and metamaterials [10].

Here, we relax the high-elevation constraint to enable simultaneous control of particle trajectories based on particle size. Partial size-dependent transport of colloidal particles has previously been demonstrated through diffusiophoresis [11–13], where variations in particle size yield distinct mobilities when the Debye screening length is comparable to the particle size [14]. Mixtures of paramagnetic beads can be sorted using magnetophoresis [15], with applications in biomagnetic separation [16–18]. Conventional magnetophoresis typically relies on static field gradients that induce motion in one direction only. Unidirectional size-dependent transport also has been achieved on mixtures of paramagnetic particles above patterned magnetic substrates and driven by a rotating magnetic field [19–21]. The rotating field induces either

---

[*] Contact author: delasheras.daniel@gmail.com; https://www.danieldelasheras.com/

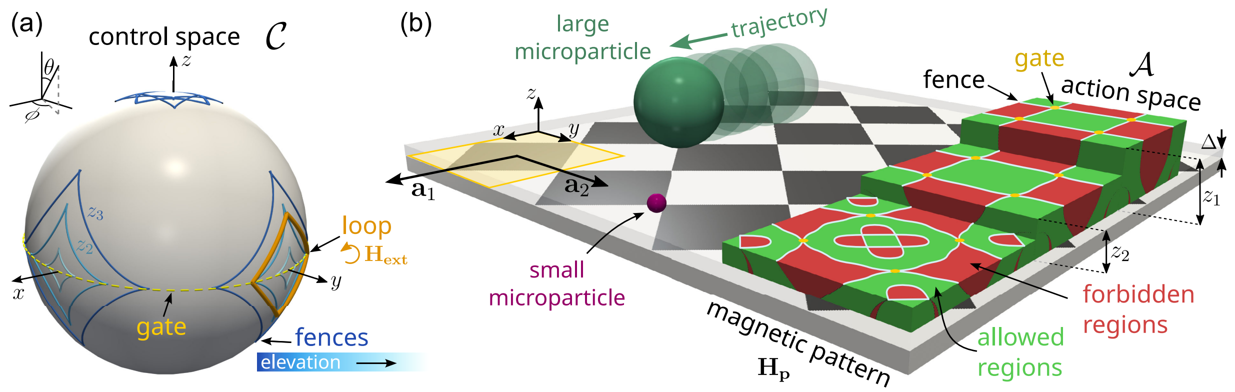

FIG. 1. Setup: (a) control space $\mathcal{C}$ and (b) action space $\mathcal{A}$. The film (b) is patterned into alternating regions of positive (black) and negative (white) magnetization along the $\hat{\mathbf{e}}_z$ direction (normal to pattern). A unit cell is highlighted in yellow. The lattice vectors $\mathbf{a}_1$ and $\mathbf{a}_2$ are parallel to $\hat{\mathbf{e}}_x$ and $\hat{\mathbf{e}}_y$, respectively. Δ is the effective thickness of the polymer coating layer. Paramagnetic microparticles (violet and green) respond to the total magnetic field: $\mathbf{H}_{\text{ext}}$ (external) and $\mathbf{H}_{\text{p}}$ (pattern). Control space $\mathcal{C}$ (a) represents all possible orientations of the uniform external field. The orientation of $\mathbf{H}_{\text{ext}}$ varies in time, tracing a closed loop (orange). The loop winds in $\mathcal{C}$ counterclockwise around the $+\mathbf{a}_2$ direction, transporting the large particles (green) along the $+\mathbf{a}_1$ direction above the pattern and leaving the small particles (purple) stationary. Allowed (green) and forbidden (red) regions at three different heights ($z_1/a = 0.375$, $z_2/a = 0.225$, and $z_3/a = 0.125$) are shown above the pattern together with their corresponding fences (white) and the gates (yellow circles). In $\mathcal{C}$, the fences are colored according to the elevation above the pattern, with darker blues representing lower elevations: z_3 (dark blue), z_2 (medium blue), z_1 (light blue). One gate corresponding to the lowest elevation is depicted as a dotted yellow line in $\mathcal{C}$.

locking current reversal of the larger particles [20] or selective chaining of the larger particles, creating dynamic channels that guide the faster motion of the smaller particles [21]. In Ref. [19], a traveling magnetic potential transports particles of different sizes depending on the driving frequency. In all these examples, the particle species move in the same direction but with significantly different speeds. A solution for complete, programmed control over distinct trajectories based on particle size has remained elusive so far.

In this Letter, we demonstrate a mechanism for complete, size-dependent control of particle trajectories, relevant in magnetically programmed microsystems [22], lab-on-a-chip technologies [23–25], and smart materials [26]. We investigate, with computer simulations and experiments, the transport of mixtures of isotropic magnetic colloidal particles above checkerboard-patterned magnetic substrates. Particles of sufficiently different sizes can be independently guided along arbitrarily complex trajectories because their heights above the pattern differ. A schematic of the setup is shown in Fig. 1, and experimental details are provided in the Supplemental Material (SM) [27]. A thin magnetic film (in the experiments, a Co/Au multilayer with a thickness of a few nanometers) is patterned into a square lattice of alternating regions of positive and negative magnetization (oriented normal to the plane of the pattern). The side length of a unit cell of the pattern, i.e., the magnitude of a lattice vector, is $a = 18$ μm. The pattern, which in the experiments is coated with a polymer film of thickness 1.5 μm that serves as a spacer, creates a position dependent magnetic field, $\mathbf{H}_{\text{p}}(\mathbf{r})$. Isotropic magnetic microparticles of diameter d_0, immersed in a solvent, sediment and reach an equilibrium elevation above the pattern, $d_0/2 + \Delta$, due to a balance between gravitational, magnetic, and DLVO forces. Here, Δ is the effective thickness of the spacer, and we assume that the particle trajectories are constrained to a plane parallel to the pattern at the equilibrium elevation. The distance between the particle surface and the coating layer depends on the particle size, but it is comparable to the Debye length, which is on the order of tens of nanometers [33], and therefore, negligible compared to the coating thickness. Hence, we approximate Δ to be the same for all particle sizes. A uniform external magnetic field $\mathbf{H}_{\text{ext}}(\hat{\boldsymbol{\omega}}) = H_{\text{ext}}\hat{\boldsymbol{\omega}}$, oriented along $\hat{\boldsymbol{\omega}}$, couples to the pattern field. The set of all possible orientations defines the surface of a sphere that we designate as control space, $\mathcal{C}$, Fig. 1(a). The external field is much stronger than $\mathbf{H}_{\text{p}}$, and its orientation, $\hat{\boldsymbol{\omega}}(t)$, varies with time, t, tracing closed loops in $\mathcal{C}$. The colloidal particles are transported by the moving minima of the total magnetic potential $V_{\text{m}}(\mathbf{r}, \hat{\boldsymbol{\omega}}) \propto -\mathbf{H}_{\text{ext}}(\hat{\boldsymbol{\omega}}) \cdot \mathbf{H}_{\text{p}}(\mathbf{r})$, which results from the coupling between the external and the pattern fields. For details on the calculation of V_{m}, see the SM [27]. For a fixed elevation, the stationary points of V_{m} divide action space $\mathcal{A}$ (i.e., the space in which the particles move) into allowed and forbidden regions for the colloidal particles that lie at that elevation; see Fig. 1(b). The minima of the potential are constrained to the allowed regions. By choosing the appropriate $\mathbf{H}_{\text{ext}}$, any point within an allowed region can be made a minimum of V_{m}. In contrast, within the forbidden regions, the only stationary points of V_{m} are saddle points. Detailed explanations of the allowed and forbidden regions are provided in Appendix A. We refer to the boundaries separating allowed and forbidden regions as fences.

The transport in the limit of large elevations above the pattern has been extensively investigated [1–3,5]. In this regime, only the first Fourier modes of the pattern field contribute significantly to the potential. For the thin pattern considered here, this high-elevation limit is effectively reached at heights comparable to the length of the unit cell size, a. At high elevation, the allowed and forbidden regions of square-patterned magnetic films form another square pattern rotated 45° with respect to that of the magnetic pattern [2,3]. Two neighboring allowed regions meet at a point in $\mathcal{A}$ that we designate as the gate; see Fig. 1(b). There exist four gates and four fences in each unit cell in $\mathcal{A}$. In control space, the fences are four points along the directions given by the lattice vectors of the pattern $\pm\hat{\mathbf{a}}_i$ with $i = 1, 2$. The gates in $\mathcal{C}$ are segments of a great circle connecting two neighboring fences. When $\mathbf{H}_{\mathrm{ext}}$ points in the direction of a gate in $\mathcal{C}$, a minimum of V_{m} appears at the position of the gate in $\mathcal{A}$. Details about the calculations of the fences and gates are provided in Appendices B and C, respectively. A loop of the orientation of $\mathbf{H}_{\mathrm{ext}}$ that winds around a fence point in $\mathcal{C}$ also crosses two different gates, and therefore, it translates the colloidal particles by one unit cell of the pattern. A loop with orientation ε winding around $\pm\hat{\mathbf{a}}_i$ in $\mathcal{C}$ transports particles by $\pm\varepsilon\hat{\mathbf{n}} \times \mathbf{a}_i$ in $\mathcal{A}$. The orientation is $\varepsilon = +1$ ($\varepsilon = -1$) for counterclockwise (clockwise) loops, and $\hat{\mathbf{n}}$ is the unit vector normal to the pattern. The set of winding numbers of the loop around the fence points in $\mathcal{C}$ uniquely determines the displacement between unit cells. Consequently, transport between unit cells is topologically protected, as it depends solely on a topological invariant, namely, the set of winding numbers.

We study here how the magnetic potential, and consequently the position of the allowed and forbidden regions as well as the fences, vary with the elevation. As the elevation decreases, the fences in $\mathcal{C}$ evolve from isolated points into closed curves that form a diamondlike contour; see Fig. 1(a) and Appendix A. The size of the diamondlike fences in $\mathcal{C}$ increases continuously with decreasing elevation. At elevations lower than $z/a \approx 0.15$, additional forbidden regions appear [Fig. 1(b)]. In $\mathcal{C}$, the corresponding fences are located close to the north pole [Fig. 1(a)]. These fences might be used to control the position within a unit cell but not for transport between unit cells. Similarly to the high-elevation limit, transport between adjacent unit cells occurs by winding around a complete diamondlike fence in $\mathcal{C}$. Illustrative particle trajectories and loops are shown in Figs. 2(a) and 2(c), respectively. The transport is adiabatic. That is, the particles follow a minimum of the potential, and therefore, they permanently stay in the allowed regions; see Fig. 2(b). The loops depicted in Fig. 2(c) start close to a gate in $\mathcal{C}$ (equator), and therefore, the starting and final positions of the particles are also near a gate in $\mathcal{A}$. Because the size of each fence varies with elevation, the transport directions of particles of different sizes can be controlled independently. A loop inside a fence does not induce transport because it crosses the gates twice and the particle returns to its initial position; see Appendix C.

Consider a loop that winds only around fences corresponding to elevations above a chosen value, z_l; see, for example, the green loop in Fig. 2(f) and the corresponding trajectories in Fig. 2(d). Such a loop transports only those particles whose centers of mass lie above z_l, i.e., particles with diameter such that $d_0/2 + \Delta > z_l$. Smaller particles, $d_0/2 + \Delta < z_l$, perform a closed trajectory and return to their original position after completion of the loop.

It is also possible to design loops that selectively transport particles within a size range $z_l > d_0/2 + \Delta > z_s$. See the violet loop in Fig. 2(f) and the induced trajectories in Fig. 2(e). The loop is formed by concatenating two subloops. The first subloop winds counterclockwise around fences with elevations higher than z_s, and hence, transports all particles with sizes $d_0/2 + \Delta > z_s$. The second subloop winds clockwise around fences with elevations above z_l, and thus, transports particles with sizes $d_0/2 + \Delta > z_l$. Crucially, the two subloops drive particle motion in opposite directions due to their opposite winding senses. Hence, only particles with sizes $z_l > d_0/2 + \Delta > z_s$ are effectively transported in the direction of the clockwise subloop, while particles with $d_0/2 + \Delta > z_l$ or $d_0/2 + \Delta < z_s$ return to their initial positions after completion of both subloops.

A collection of particles of different sizes can be controlled with these simple loops. Figures 2(g) and 2(h) illustrate the selective transport in a system with particles of three sizes. The modulation loop transports the medium-sized particle (blue) by one unit cell along the $+\mathbf{a}_2$ direction. The smallest particle (violet) follows a closed trajectory within its own unit cell, as the loop does not wind around its corresponding fence in $\mathcal{C}$. The largest particle (green) temporarily leaves its unit cell, but then, returns to its initial position because the loop winds twice, in opposite senses, around its fences in $\mathcal{C}$.

Arbitrarily complex trajectories can be generated by concatenating multiple modulation loops, as shown in Figs. 3(a) and 3(b), which compare experiments and simulations. In this example, two magnetic particles with diameters 2.8 μm and 4.5 μm are simultaneously driven by the composite modulation loop shown in Fig. 3(c): two subloops (orange and green) move large and small particles along the directions of the lattice vectors, and a third separation subloop (violet) moves only the large particles. Taking into account the thickness of the polymer coating on the pattern, the particle elevations differ by roughly 30%. The smallest particle traces the letter S, and the largest particle traces the letter L. A video of the transport is provided in the SM [27]. In the experiments, the separation

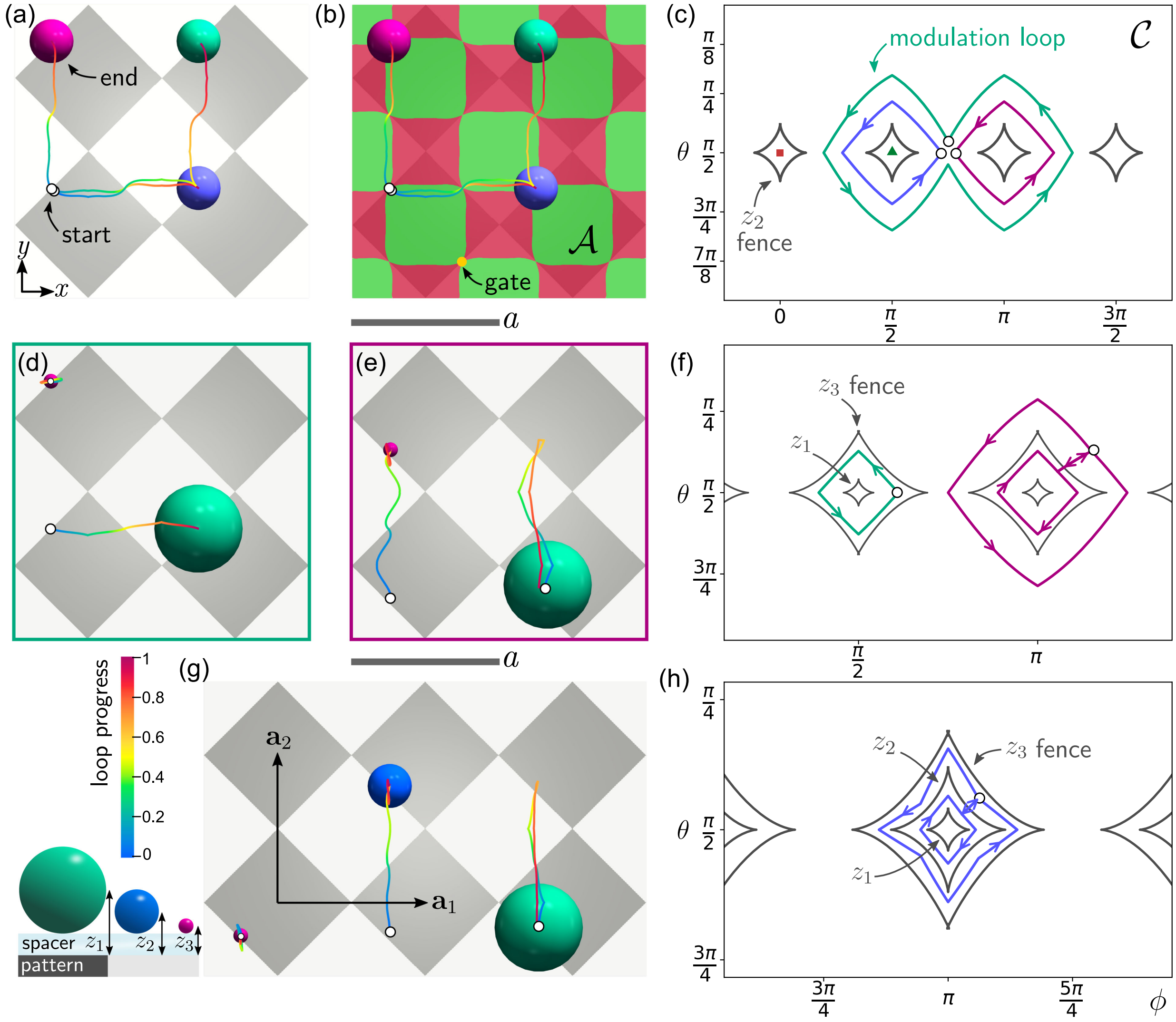

FIG. 2. Height dependent particle transport. Magnetization (a), action space, $\mathcal{A}$, with allowed (green) and forbidden (red) regions at elevation $z_2/a = 0.225$ (b), and control space, $\mathcal{C}$, mapped in Mercator projection (c). The fences (gray lines) and three modulation loops are shown in (c), with the corresponding particle trajectories from Brownian dynamics simulations depicted in (a) and (b). See details of the simulations in the SM [27]. Two loops wind around a single fence, transporting the particle by one unit cell either to the right (blue loop) or upward (violet loop). The green loop winds around two fences, transporting the particle one unit cell to the right and another one upward. The starting point of the loop in $\mathcal{C}$ and the trajectories in $\mathcal{A}$ (indicated with empty circles) are, in all cases, close to a gate (equator in $\mathcal{C}$ and a point connecting neighboring allowed regions in $\mathcal{A}$). The directions of the lattice vectors in $\mathcal{C}$ are indicated in (c): $\mathbf{a}_1 \| \hat{\mathbf{e}}_x$ (red square) and $\mathbf{a}_2 \| \hat{\mathbf{e}}_y$ (green triangle). (d),(e) Magnetization and simultaneous trajectories of two particles of different sizes, elevations $z_1/a = 0.375$ (green) and $z_3/a = 0.125$ (violet), subject to the modulation loops shown in panel (f). (d) The green loop moves the large particle one unit cell along $+\mathbf{a}_1$, leaving the final position of the small particle unaffected. (e) The violet loop moves the small particle one unit cell along $+\mathbf{a}_2$, leaving the final position of the large particle unaffected. (g) Magnetization and simultaneous trajectories of three particles of different sizes subject to the modulation loop shown in panel (h). The loop moves the medium-sized particle (blue, elevation z_2) along $+\mathbf{a}_2$ while leaving the final position of the large (green, elevation z_1) and small (violet, elevation z_3) particles unaffected. Colors along the trajectories show the progress through the loop, from start to completion (see color bar).

loop is not as robust as the other loops since it navigates between two fences. This loop has a failure rate of approximately 10%. As shown in the video, we observe more trajectories with multiple errors and relatively few with a single error. This strongly suggests that the failures are more likely due to particle-specific properties rather than the pattern or the driving protocol. The experimental fences in $\mathcal{C}$ appear to be larger than predicted theoretically. Therefore, the experimental modulation loop was adjusted accordingly; see Fig. 3(c). This discrepancy may result from several factors. For example, in the SM [27], we show that nonperfectly sharp interfaces between up- and down-magnetized domains cause an enlargement and deformation of the fences in $\mathcal{C}$. In principle, quantitative magnetic

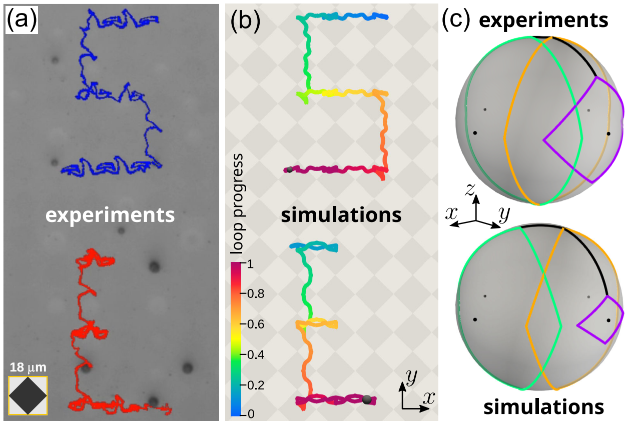

FIG. 3. Experiments on simultaneous particle transport. (a) Experimental trajectories of two particles with diameters 2.8 µm (blue) and 4.5 µm (red) subject to a unique modulation loop that controls them simultaneously. The side length of the depicted unit cell is 18 µm. The complete loop last roughly 14 minutes, and the average particle speed is approximately 0.5 µm/s. (b) Simulated trajectories colored according to the loop progress. (c) Modulation loops used in experiments and simulations. A video is available in the SM [27].

force microscopy can be used to experimentally characterize the magnetic field landscape of the pattern [34].

The ability to program the motion of individual particles based on size paves the way for new applications. As a simple proof of concept, we demonstrate that continuous size-based particle separation [35–37] can be achieved by repeatedly applying a modulation loop of gradually increasing size in control space. Such a loop sequentially activates particle motion, starting with the largest particles and extending to smaller ones as the loop winds around more fences in $\mathcal{C}$. We also construct another loop that sequentially activates the particle motion but starts with the smaller particles. Two videos demonstrating both sorting mechanisms with computer simulations are provided in the SM [27].

We have discussed the simplest, adiabatic transport mode, where particles follow a potential minimum continuously. Ratchetlike transport can occur when the loop crosses, rather than encircles, the fences (similar to high-elevation transport in other periodic patterns [1,3]). In a ratchet, the transporting minimum vanishes, and the particle rapidly relocates to a neighboring minimum. An example of ratchet motion is included in the SM [27].

Here, the motion is effectively confined to a plane. Simulations [38] and experiments [39] on related setups, but using magnetic pulses instead of homogeneous rotating fields, have revealed a hoppinglike motion, which might partially enable controlled transport in the vertical direction.

In our periodic pattern, two equal size particles at different locations always follow parallel trajectories. This limitation can be overcome with the use of nonperiodic patterns. For example, rotating a pattern also rotates its corresponding fences in $\mathcal{C}$. Hence, by constructing a pattern composed of checkerboard-patterned patches rotated relative to one another, one could control the transport according to both particle position [5] and particle size simultaneously.

Our adiabatic driving protocol offers a high degree of control over particle motion, at the cost of being significantly slower (average speed of approximately 0.5 µm/s) than other particle transport methods. Related experiments on Tb/Co multilayer patterns [40,41] have reported transport speeds of about 40 µm/s. Moreover, these patterns consist of three magnetically distinct regions, providing an additional degree of freedom for transport control.

Acknowledgments—D. d. l. H. acknowledges support through the Heisenberg program of the Deutsche Forschungsgemeinschaft (DFG, German Research Foundation) under Project No. 550390029. T. M. F. and D. d. l. H. acknowledge funding by DFG under Project No. 531559581. A. J. V. and A. E. acknowledge funding by the DFG under Projects No. 514858524, No. 566304473, No. 433501699, No. 361379292, and No. 361396165. P. K., M. U., and F. S. acknowledge financial support from the National Science Center Poland through OPUS funding (Grant No. 2020/39/B/ST5/01915).

Data availability—The data that support the findings of this article are not publicly available. The data are available from the authors upon reasonable request.

[1] J. Loehr, M. Loenne, A. Ernst, D. de las Heras, and T. M. Fischer, Topological protection of multiparticle dissipative transport, Nat. Commun. **7**, 11745 (2016).

[2] D. de las Heras, J. Loehr, M. Loenne, and T. M. Fischer, Topologically protected colloidal transport above a square magnetic lattice, New J. Phys. **18**, 105009 (2016).

[3] J. Loehr, D. de las Heras, M. Loenne, J. Bugase, A. Jarosz, M. Urbaniak, F. Stobiecki, A. Tomita, R. Huhnstock, I. Koch, A. Ehresmann, D. Holzinger, and T. M. Fischer, Lattice symmetries and the topologically protected transport of colloidal particles, Soft Matter **13**, 5044 (2017).

[4] M. Mirzaee-Kakhki, A. Ernst, D. de las Heras, M. Urbaniak, F. Stobiecki, J. Gördes, M. Reginka, A. Ehresmann, and T. M. Fischer, Simultaneous polydirectional transport of colloidal bipeds, Nat. Commun. **11**, 4670 (2020).

[5] N. C. X. Stuhlmüller, F. Farrokhzad, P. Kuświk, F. Stobiecki, M. Urbaniak, S. Akhundzada, A. Ehresmann, T. M. Fischer, and D. de las Heras, Simultaneous and independent topological control of identical microparticles in non-periodic energy landscapes, Nat. Commun. **14**, 7517 (2023).

[6] M. A. Witek, I. M. Freed, and S. A. Soper, Cell separations and sorting, Anal. Chem. **92**, 105 (2019).

[7] S. A. Kulkarni and S.-S. Feng, Effects of particle size and surface modification on cellular uptake and biodistribution

of polymeric nanoparticles for drug delivery, Pharm. Res. **30**, 2512 (2013).

[8] M. Xu, Y. Qi, G. Liu, Y. Song, X. Jiang, and B. Du, Size-dependent in vivo transport of nanoparticles: Implications for delivery, targeting, and clearance, ACS Nano **17**, 20825 (2023).

[9] Y. Zhao, L. Shang, Y. Cheng, and Z. Gu, Spherical colloidal photonic crystals, Acc. Chem. Res. **47**, 3632 (2014).

[10] J. Huh, K. Kim, E. Im, J. Lee, Y. Cho, and S. Lee, Exploiting colloidal metamaterials for achieving unnatural optical refractions, Adv. Mater. **32**, 2001806 (2020).

[11] D. Ha, S. Seo, K. Lee, and T. Kim, Dynamic transport control of colloidal particles by repeatable active switching of solute gradients, ACS Nano **13**, 12939 (2019).

[12] S. Shin, Diffusiophoretic separation of colloids in microfluidic flows, Phys. Fluids **32**, 101302 (2020).

[13] V. S. Doan, S. Chun, J. Feng, and S. Shin, Confinement-dependent diffusiophoretic transport of nanoparticles in collagen hydrogels, Nano Lett. **21**, 7625 (2021).

[14] S. Shin, E. Um, B. Sabass, J. T. Ault, M. Rahimi, P. B. Warren, and H. A. Stone, Size-dependent control of colloid transport via solute gradients in dead-end channels, Proc. Natl. Acad. Sci. U.S.A. **113**, 257 (2015).

[15] F. Alnaimat, S. Dagher, B. Mathew, A. Hilal-Alnqbi, and S. Khashan, Microfluidics based magnetophoresis: A review, Chem. Rec. **18**, 1596 (2018).

[16] J. Jung and K.-H. Han, Lateral-driven continuous magnetophoretic separation of blood cells, Appl. Phys. Lett. **93**, 223902 (2008).

[17] J. D. Adams, U. Kim, and H. T. Soh, Multitarget magnetic activated cell sorter, Proc. Natl. Acad. Sci. U.S.A. **105**, 18165 (2008).

[18] Y. Zhou, Y. Wang, and Q. Lin, A microfluidic device for continuous-flow magnetically controlled capture and isolation of microparticles, J. Microelectromech. Syst. **19**, 743 (2010).

[19] B. B. Yellen, R. M. Erb, H. S. Son, R. Hewlin, Jr, H. Shang, and G. U. Lee, Traveling wave magnetophoresis for high resolution chip based separations, Lab Chip **7**, 1681 (2007).

[20] P. Tierno, S. V. Reddy, M. G. Roper, T. H. Johansen, and T. M. Fischer, Transport and separation of biomolecular cargo on paramagnetic colloidal particles in a magnetic ratchet, J. Phys. Chem. B **112**, 3833 (2008).

[21] P. Tierno and A. V. Straube, Transport and selective chaining of bidisperse particles in a travelling wave potential, Eur. Phys. J. E **39**, 54 (2016).

[22] B. Lim, V. Reddy, X. Hu, K. Kim, M. Jadhav, R. Abedini-Nassab, Y.-W. Noh, Y. T. Lim, B. B. Yellen, and C. Kim, Magnetophoretic circuits for digital control of single particles and cells, Nat. Commun. **5**, 3846 (2014).

[23] J. Do and C. H. Ahn, A polymer lab-on-a-chip for magnetic immunoassay with on-chip sampling and detection capabilities, Lab Chip **8**, 542 (2008).

[24] M. Hejazian, W. Li, and N.-T. Nguyen, Lab on a chip for continuous-flow magnetic cell separation, Lab Chip **15**, 959 (2015).

[25] C. P. Moerland, L. J. van IJzendoorn, and M. W. J. Prins, Rotating magnetic particles for lab-on-chip applications—A comprehensive review, Lab Chip **19**, 919 (2019).

[26] F. Soto, E. Karshalev, F. Zhang, B. Esteban Fernandez de Avila, A. Nourhani, and J. Wang, Smart materials for microrobots, Chem. Rev. **122**, 5365 (2021).

[27] See Supplemental Material at http://link.aps.org/supplemental/10.1103/nvxs-n1ml for details regarding the magnetic potential, allowed and forbidden regions, fences, gates, and ratchets, which includes Refs. [28–32].

[28] C. Chappert, H. Bernas, J. Ferré, V. Kottler, J.-P. Jamet, Y. Chen, E. Cambril, T. Devolder, F. Rousseaux, V. Mathet, and H. Launois, Planar patterned magnetic media obtained by ion irradiation, Science **280**, 1919 (1998).

[29] B. Yellen, G. Friedman, and A. Feinerman, Analysis of interactions for magnetic particles assembling on magnetic templates, J. Appl. Phys. **91**, 8552 (2002).

[30] M. Urbaniak, P. Kuświk, Z. Kurant, M. Tekielak, D. Engel, D. Lengemann, B. Szymański, M. Schmidt, J. Aleksiejew, A. Maziewski, A. Ehresmann, and F. Stobiecki, Domain-wall movement control in Co/Au multilayers by He^+-ion-bombardment-induced lateral coercivity gradients, Phys. Rev. Lett. **105**, 067202 (2010).

[31] M. Urbaniak, D. Holzinger, A. Ehresmann, and F. Stobiecki, Magnetophoretic lensing by concentric topographic cylinders of perpendicular magnetic anisotropy multilayers, Biomicrofluidics **12**, 044117 (2018).

[32] P. Kuświk, A. Ehresmann, M. Tekielak, B. Szymański, I. Sveklo, P. Mazalski, D. Engel, J. Kisielewski, D. Lengemann, M. Urbaniak, C. Schmidt, A. Maziewski, and F. Stobiecki, Colloidal domain lithography for regularly arranged artificial magnetic out-of-plane monodomains in Au/Co/Au layers, Nanotechnology **22**, 095302 (2011).

[33] H. Butt, K. Graf, and M. Kappl, *Physics and Chemistry of Interfaces* (Wiley, New York, 2003).

[34] N. Zingsem, F. Ahrend, S. Vock, D. Gottlob, I. Krug, H. Doganay, D. Holzinger, V. Neu, and A. Ehresmann, Magnetic charge distribution and stray field landscape of asymmetric néel walls in a magnetically patterned exchange bias layer system, J. Phys. D **50**, 495006 (2017).

[35] J. Takagi, M. Yamada, M. Yasuda, and M. Seki, Continuous particle separation in a microchannel having asymmetrically arranged multiple branches, Lab Chip **5**, 778 (2005).

[36] J. Shi, H. Huang, Z. Stratton, Y. Huang, and T. J. Huang, Continuous particle separation in a microfluidic channel via standing surface acoustic waves (SSAW), Lab Chip **9**, 3354 (2009).

[37] X. Wang and I. Papautsky, Size-based microfluidic multimodal microparticle sorter, Lab Chip **15**, 1350 (2015).

[38] F. Klingbeil, F. Block, U. Sajjad, R. B. Holländer, S. Deshpande, and J. McCord, Evaluating and forecasting movement patterns of magnetically driven microbeads in complex geometries, Sci. Rep. **10**, 8761 (2020).

[39] R. Huhnstock, M. Reginka, C. Sonntag, M. Merkel, K. Dingel, B. Sick, M. Vogel, and A. Ehresmann, Three-dimensional close-to-substrate trajectories of magnetic microparticles in dynamically changing magnetic field landscapes, Sci. Rep. **12**, 20890 (2022).

[40] M. Urbaniak, D. Kiphart, M. Matczak, F. Stobiecki, G. D. Chaves-O'Flynn, and P. Kuświk, Ferrimagnetic Tb/Co multilayers patterned by ion bombardment as substrates for magnetophoresis, Sci. Rep. **14**, 23771 (2024).

[41] M. Urbaniak, D. Kiphart, M. Matczak, and P. Kuświk, Reconfigurable ferrimagnetic Tb/Co based substrates for magnetophoresis, J. Magn. Magn. Mater. **629**, 173312 (2025).

End Matter

Appendix A: Allowed and forbidden regions—In the experiments, gravitational and magnetic forces attract the particles toward the polymer coating. Adhesion of the particles to the surface is prevented by the repulsive screened electrostatic interaction between the polymer coating and the particles. As a result, the colloidal beads levitate above the coating at a distance comparable to the Debye length, which we estimate to be on the order of tens of nanometers and, therefore, negligible compared with the thickness of the polymer coating. Hence, the particle transport is governed by the stationary points of the magnetic potential at a fixed elevation, i.e., by those points satisfying

$$\nabla_{\mathcal{A}} V_{\mathrm{m}}(\mathbf{r}, \hat{\boldsymbol{\omega}}) = 0. \tag{A1}$$

Here, we define $\nabla_{\mathcal{A}} = (\nabla_x, \nabla_y, 0)$. Because the particles move at constant elevation, we do not need to consider the effect of the magnetic force along the direction normal to the pattern (z-axis). The set of minima of the potential defines the allowed regions, whereas the set of saddle points defines the forbidden regions.

Since the potential $V_{\mathrm{m}}(\mathbf{r}, \hat{\boldsymbol{\omega}}) \propto -\mathbf{H}_{\mathrm{ext}}(\hat{\boldsymbol{\omega}}) \cdot \mathbf{H}_{\mathrm{p}}(\mathbf{r})$ (see SM [27]), a minimum of V_{m} at position $\mathbf{r}$ can be converted into a maximum at the same position by inverting the orientation of the external field. That is, the transformation $\hat{\boldsymbol{\omega}} \to -\hat{\boldsymbol{\omega}}$. Therefore, both minima and maxima of the potential correspond to allowed regions. At any position $\mathbf{r}$ within an allowed region, there exists an orientation of the external field that renders $\mathbf{r}$ a minimum (or a maximum) of V_{m}. In contrast, in the forbidden regions, the only stationary points of V_{m} are saddle points.

It follows from Eq. (A1) that the external field that makes a given position $\mathbf{r}$ stationary satisfies

$$\mathbf{H}_{\mathrm{ext}}(\hat{\boldsymbol{\omega}}) \cdot \nabla_\alpha \mathbf{H}_{\mathrm{p}}(\mathbf{r}) = 0, \quad \alpha = \{x, y\}. \tag{A2}$$

According to Eq. (A2), the point $\mathbf{r}$ is stationary if the external field is parallel to

$$\mathbf{H}_{\mathrm{sta}}(\mathbf{r}) = \pm \nabla_x \mathbf{H}_{\mathrm{p}}(\mathbf{r}) \times \nabla_y \mathbf{H}_{\mathrm{p}}(\mathbf{r}). \tag{A3}$$

Equation (A3) is valid except for the special case $\nabla_x \mathbf{H}_{\mathrm{p}} \| \nabla_y \mathbf{H}_{\mathrm{p}}$, which is discussed later.

To determine whether a point $\mathbf{r}$ at fixed elevation belongs to an allowed or forbidden region, we align the external field $\mathbf{H}_{\mathrm{ext}}$ with the stationary direction $\mathbf{H}_{\mathrm{sta}}$, Eq. (A3), and evaluate the Hessian matrix of the magnetic potential V_{m},

$$\nabla_{\mathcal{A}} \nabla_{\mathcal{A}} V_{\mathrm{m}} \propto -\begin{pmatrix} \mathbf{H}_{\mathrm{sta}} \cdot \nabla_x \nabla_x \mathbf{H}_{\mathrm{p}} & \mathbf{H}_{\mathrm{sta}} \cdot \nabla_x \nabla_y \mathbf{H}_{\mathrm{p}} \\ \mathbf{H}_{\mathrm{sta}} \cdot \nabla_y \nabla_x \mathbf{H}_{\mathrm{p}} & \mathbf{H}_{\mathrm{sta}} \cdot \nabla_y \nabla_y \mathbf{H}_{\mathrm{p}} \end{pmatrix}, \tag{A4}$$

where constant multiplicative factors are omitted, as they play no role in the current discussion. The point $\mathbf{r}$ lies in an allowed region if the determinant of the Hessian is positive and in a forbidden region if it is negative.

Plots of the allowed and forbidden regions are shown in Fig. 4. At elevations larger than the length of a lattice vector, $z \gtrsim a$, the allowed and forbidden regions form an almost perfect square pattern rotated 45° with respect to the magnetization pattern. By decreasing the elevation, first the regions get only slightly distorted; see Fig. 4(a). At elevations below $z/a \approx 0.15$, the deformation is noticeable, and new forbidden regions start to appear inside the allowed regions. Nevertheless, it is still possible to move from one unit cell to any of the neighboring unit cells through allowed regions. Therefore, there must exist a loop in $\mathcal{C}$ that transports a minimum of the magnetic potential to the desired unit cell.

Appendix B: Fences—The fences in action space are the boundaries between the allowed and the forbidden regions. At the fences, an eigenvalue of the Hessian matrix, Eq. (A4), is zero, and the determinant vanishes. We find the fences in $\mathcal{A}$ numerically by looking at those points for which the determinant changes sign using a simple bisection method. Once the fences in $\mathcal{A}$ are found, we obtain the corresponding fences in control space by calculating the stationary direction at the fence via Eq. (A3). In the infinite-height limit, the fences in $\mathcal{C}$ reduce to points in checkerboard patterns because the magnetic potential decomposes into a sum of two magnetic potentials, one depending only on x and the other depending only on y. When the external field points toward a fence, say in the x-direction, the minimum of the colloidal potential in $\mathcal{A}$ forms a flat valley along the y-direction, a Goldstone mode [2,3]. At finite height, more than one Fourier mode contributes to V_{m}, and the separation of variables no longer holds. The Goldstone mode disappears, and the fences in $\mathcal{C}$ are no longer points but curves consisting of four joined segments.

Plots of the fences in action space and control space at three different elevations are shown in Figs. 4(a) and 4(b), respectively. In the infinite-height limit, the point fences in $\mathcal{C}$ are located along the directions of the lattice vectors $\pm\hat{\mathbf{a}}_i$, with $i = \{1, 2\}$. As the height decreases, the fences in $\mathcal{C}$

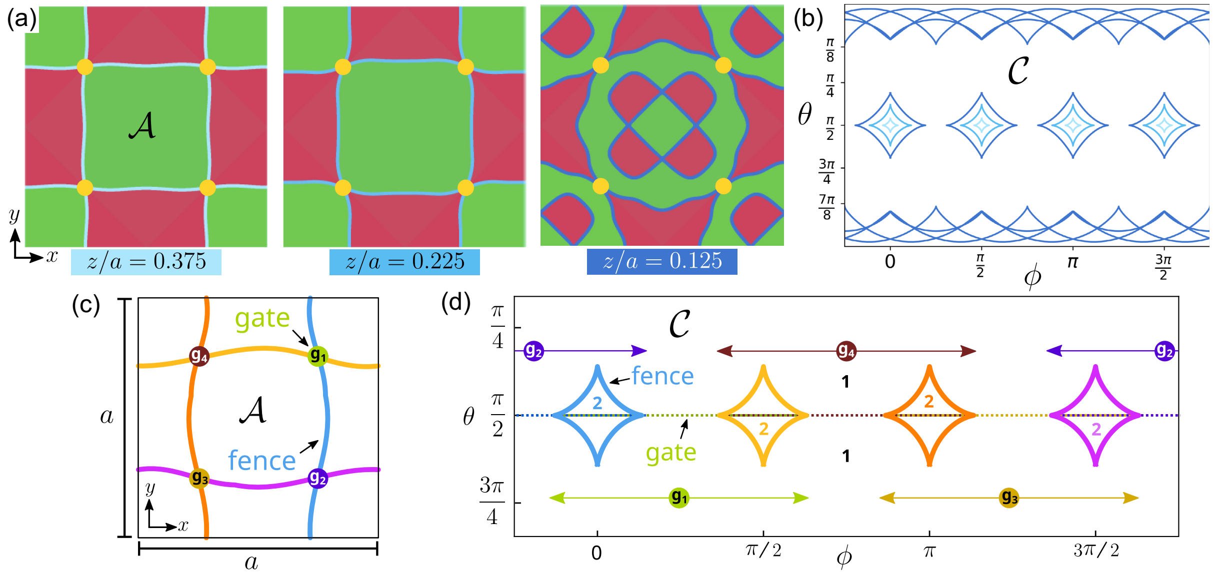

FIG. 4. Action and control spaces. (a) One unit cell in action space and (b) the corresponding control space (Mercator projection) of a checkerboard magnetic pattern at three elevations: $z/a = 0.375$, $z/a = 0.225$, and $z/a = 0.125$. The gates connecting two allowed regions of neighboring unit cells in $\mathcal{A}$ are indicated with yellow circles, the fences with blue lines, and the allowed and forbidden regions are colored in green and red, respectively. The color of the fences in $\mathcal{C}$ indicates the elevation above the pattern: $z/a = 0.375$ (dark blue), $z/a = 0.225$ (medium blue), and $z/a = 0.125$ (light blue). Fences and gates for elevation $z/a = 0.2$ in (c) action space and (d) control space. Fences and gates are colored consistently across panels (c) and (d) to indicate the same objects represented in $\mathcal{A}$ and $\mathcal{C}$. The fences are represented as solid lines in both $\mathcal{A}$ and $\mathcal{C}$. The gates are indicated by the circles labeled g_i with $i = 1, \ldots, 4$ in $\mathcal{A}$ and by dotted lines in $\mathcal{C}$. The arrows in (d) indicate the angular width of the respective gate. Each gate connects two opposite vertices of neighboring fences. The digits in (d) indicate the number of minima of V_{m} per unit cell in $\mathcal{A}$ for each region in $\mathcal{C}$: two minima inside the diamondlike fences and one minimum outside. The angles in (b) and (d) are expressed in radians.

deform into diamondlike closed curves whose sizes increase monotonically as the pattern is approached. In the limit $z \to 0$, neighboring diamond-shaped fences touch each other in $\mathcal{C}$. The angular width of these diamond-shaped fences as a function of elevation is shown in the SM [27].

At low elevations, secondary fences appear in $\mathcal{C}$; see Fig. 4(b). These correspond to the boundaries between forbidden and allowed regions that emerge inside the unit cell; see, for instance, the action space at elevation $z/a = 0.125$ in Fig. 4(a). However, these secondary fences are not directly involved in the particle transport between different unit cells. When $\mathbf{H}_{\mathrm{ext}}$ points to the north pole of $\mathcal{C}$, the magnetic potential has a minimum (at any height) at the center of an up-magnetized pattern tile. Hence, forbidden regions cannot form at the center of the allowed region. Due to fourfold rotational symmetry, forbidden regions must appear in sets of four, and when they are connected, symmetry requires the resulting fences to encircle the north pole of $\mathcal{C}$.

Appendix C: Gates—The gates in $\mathcal{A}$ correspond to the points connecting two neighboring allowed regions [yellow circles in Fig. 4(a)]. At a gate in $\mathcal{A}$, two different fences intersect, implying that there must exist at least two directions of $\mathbf{H}_{\mathrm{ext}}$ that render the gate a stationary point of V_{m}. For this condition to hold, the vectors $\nabla_x \mathbf{H}_{\mathrm{p}}$ and $\nabla_y \mathbf{H}_{\mathrm{p}}$ must be parallel, since the stationary direction given in Eq. (A3) is determined by their cross product. Therefore, at a gate $\nabla_x \mathbf{H}_{\mathrm{p}} \| \nabla_y \mathbf{H}_{\mathrm{p}}$ and $\mathbf{H}_{\mathrm{sta}} \perp \nabla_\alpha \mathbf{H}_{\mathrm{p}}$ with $\alpha = \{x, y\}$. In other words, any external field perpendicular to $\nabla_\alpha \mathbf{H}_{\mathrm{p}}$ renders the gate in $\mathcal{A}$ a stationary point. Hence, a gate in $\mathcal{C}$ is a great circle. However, not all orientations of $\mathbf{H}_{\mathrm{ext}}$ along this great circle produce a potential minimum at the gate in $\mathcal{A}$. Depending on the specific orientation, the gate in $\mathcal{A}$ may correspond to a minimum, a saddle point, or a maximum of the potential. A gate in $\mathcal{C}$ represents a minimum in $\mathcal{A}$ only for those orientations of $\mathbf{H}_{\mathrm{ext}}$ along the great circle for which both eigenvalues of the Hessian matrix, Eq. (A4), are positive. This condition is satisfied only within a segment of the great circle that defines the gate in $\mathcal{C}$.

The gates that connect allowed regions of neighboring unit cells in $\mathcal{A}$ [those highlighted in Fig. 4(a)] lie on the equator of $\mathcal{C}$ (which corresponds to orientations of $\mathbf{H}_{\mathrm{ext}}$ parallel to the plane of the pattern). Figures 4(c) and 4(d) show the gates in both $\mathcal{A}$ and $\mathcal{C}$, respectively, for an intermediate elevation. In the infinite height limit [2], the segment of each gate in $\mathcal{C}$ that corresponds to potential minima connects two adjacent fence points in $\mathcal{C}$. These two fences are precisely those that intersect in $\mathcal{A}$. At intermediate elevations, the corresponding gate segments connect two opposite vertices of adjacent diamondlike fences. A simple modulation loop that winds once around a complete fence in $\mathcal{C}$ crosses two different gates. The corresponding loop in $\mathcal{A}$ transports a minimum of the magnetic potential through these gates, thereby inducing particle transport (provided that the minimum is initially occupied by a colloidal particle). A loop lying entirely within a diamondlike fence can be contracted to a point in $\mathcal{C}$, which is equivalent to a static external field. Hence, such a loop cannot induce particle transport. When $\mathbf{H}_{\text{ext}}$ points inside a fence, V_{m} has two minima per unit cell in $\mathcal{A}$, whereas only one minimum exists when $\mathbf{H}_{\text{ext}}$ points outside the fence. A loop inside the fence crosses two gates, but each gate is crossed twice; see Fig. 4(d). In $\mathcal{A}$, one minimum of V_{m} crosses one gate twice, and the other minimum also crosses the other gate twice. As a result, a particle following either minimum undergoes no net transport after the loop is completed.